Multiple Image Technique (MIT) and Anistropic Perfectly Matched Layer (APML) in Implementation of MRTD Scheme for Boundary Truncations of Microwave Structures

Qunsheng Cao, Yinchao Chen, *Member, IEEE*, and Raj Mittra, *Life Fellow, IEEE*

***Abstract*—This paper presents an adjustable multiple image technique (MIT) and an anisotropic perfectly matched layer (APML) employed in the context of multiresolution time-domain (MRTD) scheme for the truncation of the computational boundary, with the MIT used for perfect electrically conducting (PEC) shields and the APML for open structures. We begin by presenting a systematic formulation for developing the constitutive relations and update equations in the transform domain of the MRTD, when considering both the original and image regions. We then illustrate the applications of the above techniques by analyzing a two-layer dielectric-loaded cavity, printed circuit enclosed by a PEC, as well as open transmission lines. Although, in principle, one can employ a large number of images to ensure the accuracy of the MRTD computation, in practice, it is useful, from the point-of-view of computational efficiency, to develop a criterion that determines the number of requisite images. While its formulation may appear to be lengthy, the MIT is based on physical concepts that are fairly well suited for computer programming, it places relatively little additional burden on the memory requirement. In addition, it provides the user the flexibility of choosing the number of images along each side of the structure. The computed results for all cases investigated show excellent agreement with those obtained by using other techniques, and yet, the demand on the computational resources in the MRTD is much less than that needed in the finite-difference time-domain algorithm.**

***Index Terms*—Anisotropic perfectly matched layer, dielectric-loaded cavity, multiple image technique, multiresolution time-domain scheme, printed transmission line.**

I. Introduction

THE multiresolution time domain (MRTD) scheme for solving electromagnetic-field problems, introduced by Krumpholz and Katehi [1] and Robertson *et al.* [2], is based on expansions of unknown fields in terms of scaling or wavelet functions. It has been shown that the use of the MRTD improves the computational capacity and efficiency over those of the conventional finite-difference time-domain (FDTD) method [1]–[5]. Although the concept of image theory for truncating a computational domain bounded by perfect electric conductors (PECs) has been introduced previously in the context of MRTD [1], the procedure for generating these images on different sides of a structure is neither obvious, nor straightforward, particularly when complex materials and multiple images are involved.

The MRTD approach described in this paper is different from those published previously in the following two ways. First, we retain the philosophy of the leapfrog algorithm employed in the conventional FDTD and place the MRTD scheme in the context of the FDTD. Second, we present a systematic approach, referred to here as the multiple image technique (MIT), for incorporating the image theory in the MRTD scheme for boundary truncation of PEC-shielded structures. The primary motivation behind introducing the MIT is to provide the user with the flexibility to vary the number of side images, and thereby strike a balance between accuracy and memory saving. An obvious advantage is that the additional images do not require additional memory in the MIT–MRTD implementation. We illustrate the application of the MIT by analyzing a two-layer dielectric-loaded cavity, and develop a systematic formulation for constructing the constitutive relations and update equations in the MRTD transform domain by utilizing only the field quantities defined in the real structures. Furthermore, we present a criterion for determining the number of images needed along each side of the structure that is based on the localization properties of the scaling basis functions. Although, in principle, we can construct as many images as we desire, it is highly desirable to limit their number from the point-of-view of balancing the numerical efficiency and accuracy.

In this paper, we also present a two-dimensional (2-D) version of the MRTD, in conjunction with the unsplit anisotropic perfectly matched layer (APML), for the analysis of printed transmission lines. We apply the MIT-APML concept for the analysis of microwave structures with inhomogeneous materials, including different dielectrics and conductors with infinite conductivity. Such imaging is needed to handle the boundaries in the MRTD formulation.

Manuscript received August 14, 1998. This work was supported in part by the Hong Kong Polytechnic University under Grant G-V674.

Q. Cao is with the Department of Electronic and Information Engineering, Hong Kong Polytechnic University, Hong Kong.

Y. Chen is with the Department of Electrical Engineering, University of South Carolina, Columbia, SC 29208 USA.

R. Mittra is with the Electrical Engineering Department, Pennsylvania State University, University Park, PA 16802 USA.

Publisher Item Identifier S 0018-9480(02)05221-3.

II. MIT–MRTD Method for PEC-Shielded Structures

A. MRTD Update Equations

By using the generalized differential matrix operators (GDMOs) [6], the two curl relations of the Maxwell's equations can be expressed as

$$\begin{bmatrix} 0 & -\partial_z & \partial_y \\ \partial_z & 0 & -\partial_x \\ -\partial_y & \partial_x & 0 \end{bmatrix} \begin{bmatrix} H_x \\ H_y \\ H_z \end{bmatrix} = \frac{\partial}{\partial t} \begin{bmatrix} D_x \\ D_y \\ D_z \end{bmatrix} \tag{1}$$

$$\begin{bmatrix} 0 & -\partial_z & \partial_y \\ \partial_z & 0 & -\partial_x \\ -\partial_y & \partial_x & 0 \end{bmatrix} \begin{bmatrix} E_x \\ E_y \\ E_z \end{bmatrix} = -\mu_0 \frac{\partial}{\partial t} \begin{bmatrix} H_x \\ H_y \\ H_z \end{bmatrix} \tag{2}$$

where, for generality, we assume that the relative permittivity is a biaxial tensor. The associated constitutive relation in the space domain then becomes

$$\begin{bmatrix} D_x \\ D_y \\ D_z \end{bmatrix} = \varepsilon_0 \begin{bmatrix} \varepsilon_{xx}(\vec{r}) & 0 & 0 \\ 0 & \varepsilon_{yy}(\vec{r}) & 0 \\ 0 & 0 & \varepsilon_{zz}(\vec{r}) \end{bmatrix} \begin{bmatrix} E_x \\ E_y \\ E_z \end{bmatrix}. \tag{3}$$

In the MRTD domain, the above local relationship between D- and E-fields is no longer valid; hence, we must work simultaneously with both the D- and E-fields.

As a first step in the MRTD formulation, we begin by representing all the field quantities in terms of the scaling function in space and pulse function in time as follows:

$$D_x(\vec{r},t) = \sum_{i,j,k,n=-\infty}^{\infty} {}_{\phi x}D^n_{i+\frac{1}{2},j,k}\phi_{i+\frac{1}{2}}(x)\phi_j(y)\phi_k(z)h_n(t) \tag{4}$$

$$H_x(\vec{r},t) = \sum_{i,j,k,n=-\infty}^{\infty} {}_{\phi x}H^n_{i,j+\frac{1}{2},k+\frac{1}{2}}\phi_i(x)\phi_{j+\frac{1}{2}}(y)\phi_{k+\frac{1}{2}}(z)h_{n+\frac{1}{2}}(t) \tag{5}$$

where $\phi(x)$ denotes the cubic spline Battle–Lemarie scaling function [7], [8], and $h_n(t)$ is a rectangular pulse function. Substitution of the above field expansions into the Maxwell's equations, followed by the application of the Galerkin's method [9], leads us to the following set of update equations:

$$\begin{aligned} {}_{\phi x}D^{n+1}_{i+\frac{1}{2},j,k} &= {}_{\phi x}D^n_{i+\frac{1}{2},j,k} \\ &\quad + \sum_{\nu} a(\nu)\left[{}_{\phi z}H^{n+\frac{1}{2}}_{i+\frac{1}{2},j+\nu+\frac{1}{2},k}\frac{\Delta t}{\Delta y} - {}_{\phi y}H^{n+\frac{1}{2}}_{i+\frac{1}{2},j,k+\nu+\frac{1}{2}}\frac{\Delta t}{\Delta z}\right] \end{aligned} \tag{6}$$

$$\begin{aligned} {}_{\phi x}H^{n+\frac{1}{2}}_{i,j+\frac{1}{2},k+\frac{1}{2}} &= {}_{\phi x}H^{n-\frac{1}{2}}_{i,j+\frac{1}{2},k+\frac{1}{2}} \\ &\quad + \frac{1}{\mu_0}\sum_{\nu} a(\nu)\left[{}_{\phi y}E^n_{i,j+\frac{1}{2},k+\nu+1}\frac{\Delta t}{\Delta z} - {}_{\phi z}E^n_{i,j+\nu+1,k+\frac{1}{2}}\frac{\Delta t}{\Delta y}\right] \end{aligned} \tag{7}$$

where the quantities being updated are the expansion coefficients in the field expansions, and their corresponding superscripts and subscripts represent the discretized time and space positions, respectively. The coefficient $a(\nu)$, appearing in (6) and (7), may be derived by utilizing a nonorthogonal relationship [1], [4]. Although the summation index ν in (6) and (7) spans from positive to negative infinity, it is usually sufficient to truncate it at nine, by taking advantage of the localized nature of the Battle–Lemarie scaling function.

B. MIT for the Derivation of the Constitutive Relationship

The constitutive relationship in the transform domain of the MRTD is considerably more involved than its counterpart in the spatial domain presented in (3). This is because the MRTD-transformed D-field at a particular point is determined not only by the E-field at the same location, but also by the distribution of the E-field in its neighborhood. To solve for the constitutive relation in the MRTD domain, we once again represent the E-fields as expansions in terms of the same basis functions as (4), and substitute the above expansion into (3). Next, an application of the Galerkin's method leads us to the constitutive relationships in the MRTD domain that read

$${}_{\phi x}D^n_{i+\frac{1}{2},j,k} = \varepsilon_0 \sum_{i',j',k'=-\infty}^{+\infty} (\varepsilon_{xx})_{ii',jj',kk'}\,{}_{\phi x}E^n_{i'+\frac{1}{2},j',k'} \tag{8}$$

where

$$\begin{aligned} (\varepsilon_{xx})_{ii',jj',kk'} &= \int_{-\infty}^{+\infty}\int_{-\infty}^{+\infty}\int_{-\infty}^{+\infty} \phi_{i+\frac{1}{2}}(x)\phi_j(y)\phi_k(z)\varepsilon_{xx}(\vec{r}) \\ &\quad \times \phi_{i'+\frac{1}{2}}(x)\phi_{j'}(y)\phi_k(z)\frac{dx\,dy\,dz}{\Delta x\,\Delta y\,\Delta z} \\ &= \delta_{i,i'}\delta_{j,j'}\delta_{k,k'} + \sum_{p=1}^{P}\left[\varepsilon_{xx}(p)-1\right]\xi_{ii',jj',kk'}(p) \end{aligned} \tag{9a}$$

$$\begin{aligned} \xi_{ii'jj'kk'} &= \alpha_{i,i'}(p)\beta_{j,j'}(p)\gamma_{k,k'}(p) \\ &= \int_{x_1(p)}^{x_2(p)} \phi_{i+\frac{1}{2}}(x)\phi_{i'+\frac{1}{2}}(x)\frac{dx}{\Delta x} \\ &\quad \times \int_{y_1(p)}^{y_2(p)} \phi_j(y)\phi_{j'}(y)\frac{dy}{\Delta y}\int_{z_1(p)}^{z_2(p)} \phi_k(z)\phi_k(z)\frac{dz}{\Delta z} \end{aligned} \tag{9b}$$

where we assume all dielectric objects are rectangular, and P is the total number of dielectric objects.

We now present an example of deriving the constitutive relationship for a two-layer dielectric-loaded cavity, shown in Fig. 1. By expressing

$$\begin{aligned} \varepsilon_{\alpha\alpha} &= \varepsilon_{\alpha\alpha}(y) \\ &= \begin{cases} \varepsilon_r(p), & y_1(p) \le y \le y_2(p) \\ 1, & \text{otherwise} \end{cases} \qquad (p=1,2) \end{aligned} \tag{10}$$

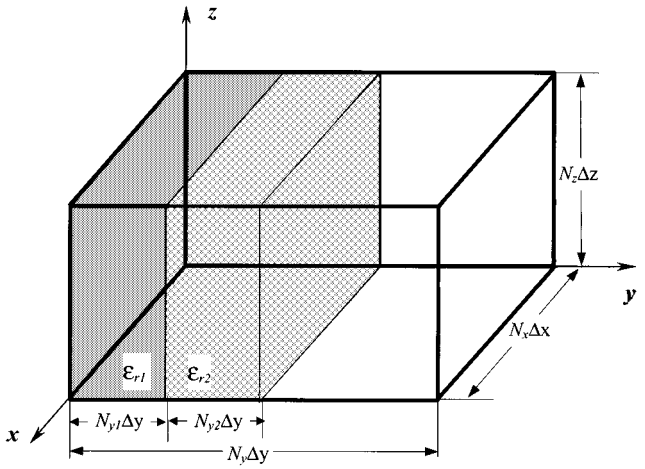

Fig. 1. Geometry of a two-layer dielectric-loaded cavity.

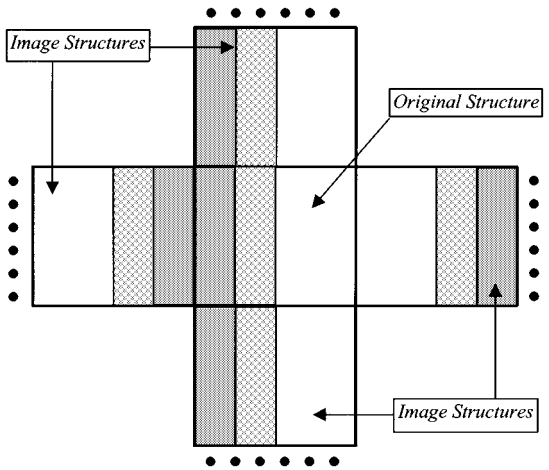

Fig. 2. Original structure and multiple images in the y–z-plane.

we can write the x-component of the constitutive relation in the MRTD domain

$$\phi x D^n_{i+\frac{1}{2},j,k} = \varepsilon_0 \sum_{j'=j-M}^{j+M} (\varepsilon_{xx})_{j,j'} \phi x E^n_{i+\frac{1}{2},j',k} \tag{11}$$

with

$$(\varepsilon_{xx})_{j,j'} = \delta_{j,j'} + \sum_{p=1}^{P} [\varepsilon_r(p) - 1] \int_{y_1(p)}^{y_2(p)} \phi_j(y)\phi_{j'}(y) \frac{dy}{\Delta y} \tag{12}$$

where M is the number of the sampled E-fields in the MRTD domain. It is usually set equal to a number slightly greater than nine by taking advantage of the localization of the scaling function.

It is very important to note that the summations in (11) not only cover the original computation domain, but also the entire image regions, as shown in Fig. 2. In fact, for a PEC-shielded structure, all of the field quantities in the image regions can be expressed in terms of the ones inside the original cavity structure. Toward this end, we employ the following principle. The tangential components of the image E-fields (parallel to the PEC mirror wall) or the normal components of the image H-fields (normal to the PEC mirror wall) are always odd symmetric about the original fields, while the normal components of the image E-fields and the tangential components of the image H-fields are even symmetric. Using the above guidelines, we can express all of the image field quantities in terms of the fields in the original region, and this leads to a degeneration of the summation index in (11) to N_y, the grid number along the y-direction, defined only inside the original cavity structure. Consequently, (11) can be simplified to read

$$\phi x D^n_{i+\frac{1}{2},j,k} = \varepsilon_0 \sum_{j'=0}^{N_y} (\hat{\varepsilon}_{xx})_{j,j'} \phi x E^n_{i+\frac{1}{2},j',k} \tag{13}$$

where we define the equivalent permittivity matrix in the MRTD domain as follows:

$$\begin{aligned}\sum_{j'=0}^{N_y} (\hat{\varepsilon}_{xx})_{j,j} = {} & \sum_{j'=0}^{N_y} (\varepsilon_{xx})_{j,j'} - \sum_{j'=-1}^{-N_y} (\varepsilon_{xx})_{j,j'} \\ & - \sum_{j'=N_y+1}^{2N_y} (\varepsilon_{xx})_{j,j'} - \cdots + (-1)^m \\ & \times \sum_{j'=-(m-1)N_y-1}^{j-M} (\varepsilon_{xx})_{j,j'} + (-1)^m \\ & \times \sum_{j'=mN_y+1}^{j+M} (\varepsilon_{xx})_{j,j'}\end{aligned} \tag{14a}$$

or in a matrix form as

$$\begin{aligned}[\hat{\varepsilon}_{xx}] = {} & [\varepsilon_{xx}]_{\text{Orig}} - [\varepsilon_{xx}]_{\text{Img}(-1)} - [\varepsilon_{xx}]_{\text{Img}(+1)} - \cdots \\ & + (-1)^m [\varepsilon_{xx}]_{\text{Img}(-m)} + (-1)^m [\varepsilon_{xx}]_{\text{Img}(+m)}\end{aligned} \tag{14b}$$

where the m is the number of images. The first term in (14b) corresponds to the original structure, and the rest are associated with the images.

Next, we present a criterion for determining the number of image m, along the y-direction (positive or negative). The criterion is derived from the knowledge of the effective range of the basis functions at the PEC boundary locations as follows:

$$m = \begin{cases} \text{INT}\left[\dfrac{M}{N_y}\right] + 1, & \text{if } \dfrac{M}{N_y} \text{ is not an integer} \\ \dfrac{M}{N_y}, & \text{if } \dfrac{M}{N_y} \text{ is an integer} \end{cases} \tag{15}$$

where INT is the integer-converting function that truncates all the decimal parts of a number. For example, if $M = 10, N_y = 4, m = \text{INT}(2.5) + 1 = 3$, this implies that we need three images in both sides of the $+y$- and $-y$-directions.

We will now illustrate the procedure for deriving the equivalent permittivity matrix in the MRTD domain. We consider a

cavity with the discretization grid number $N_y = 6$ in the y-direction. For the sake of simplifying the notation, we omit the subscript x, and write $(\varepsilon_{xx})_{j,j}$ simply as $\varepsilon_{j,j'}$. In this example, we choose $M = 9$ and $m = 2$. We then have

$$\begin{bmatrix} \phi x D^n_{i+\frac{1}{2},0,k} \\ \phi x D^n_{i+\frac{1}{2},1,k} \\ \phi x D^n_{i+\frac{1}{2},2,k} \\ \phi x D^n_{i+\frac{1}{2},3,k} \\ \phi x D^n_{i+\frac{1}{2},4,k} \\ \phi x D^n_{i+\frac{1}{2},5,k} \\ \phi x D^n_{i+\frac{1}{2},6,k} \end{bmatrix} = \varepsilon_0 \begin{bmatrix} \hat{\varepsilon}_{0,0} & \hat{\varepsilon}_{0,1} & \hat{\varepsilon}_{0,2} & \hat{\varepsilon}_{0,3} & \hat{\varepsilon}_{0,4} & \hat{\varepsilon}_{0,5} & \hat{\varepsilon}_{0,6} \\ \hat{\varepsilon}_{1,0} & \hat{\varepsilon}_{1,1} & \hat{\varepsilon}_{1,2} & \hat{\varepsilon}_{1,3} & \hat{\varepsilon}_{1,4} & \hat{\varepsilon}_{1,5} & \hat{\varepsilon}_{1,6} \\ \hat{\varepsilon}_{2,0} & \hat{\varepsilon}_{2,1} & \hat{\varepsilon}_{2,2} & \hat{\varepsilon}_{2,3} & \hat{\varepsilon}_{2,4} & \hat{\varepsilon}_{2,5} & \hat{\varepsilon}_{2,6} \\ \hat{\varepsilon}_{3,0} & \hat{\varepsilon}_{3,1} & \hat{\varepsilon}_{3,2} & \hat{\varepsilon}_{3,3} & \hat{\varepsilon}_{3,4} & \hat{\varepsilon}_{3,5} & \hat{\varepsilon}_{3,6} \\ \hat{\varepsilon}_{4,0} & \hat{\varepsilon}_{4,1} & \hat{\varepsilon}_{4,2} & \hat{\varepsilon}_{4,3} & \hat{\varepsilon}_{4,4} & \hat{\varepsilon}_{4,5} & \hat{\varepsilon}_{4,6} \\ \hat{\varepsilon}_{5,0} & \hat{\varepsilon}_{5,1} & \hat{\varepsilon}_{5,2} & \hat{\varepsilon}_{5,3} & \hat{\varepsilon}_{5,4} & \hat{\varepsilon}_{5,5} & \hat{\varepsilon}_{5,6} \\ \hat{\varepsilon}_{6,0} & \hat{\varepsilon}_{6,1} & \hat{\varepsilon}_{6,2} & \hat{\varepsilon}_{6,3} & \hat{\varepsilon}_{6,4} & \hat{\varepsilon}_{6,5} & \hat{\varepsilon}_{6,6} \end{bmatrix} \times \begin{bmatrix} \phi x E^n_{i+\frac{1}{2},0,k} \\ \phi x E^n_{i+\frac{1}{2},1,k} \\ \phi x E^n_{i+\frac{1}{2},2,k} \\ \phi x E^n_{i+\frac{1}{2},3,k} \\ \phi x E^n_{i+\frac{1}{2},4,k} \\ \phi x E^n_{i+\frac{1}{2},5,k} \\ \phi x E^n_{i+\frac{1}{2},6,k} \end{bmatrix} \tag{16}$$

with

$$[\varepsilon_{xx}]_{\text{Orig}} = \begin{bmatrix} \varepsilon_{0,0} & \varepsilon_{0,1} & \varepsilon_{0,2} & \varepsilon_{0,3} & \varepsilon_{0,4} & \varepsilon_{0,5} & \varepsilon_{0,6} \\ \varepsilon_{1,0} & \varepsilon_{1,1} & \varepsilon_{1,2} & \varepsilon_{1,3} & \varepsilon_{1,4} & \varepsilon_{1,5} & \varepsilon_{1,6} \\ \varepsilon_{2,0} & \varepsilon_{2,1} & \varepsilon_{2,2} & \varepsilon_{2,3} & \varepsilon_{2,4} & \varepsilon_{2,5} & \varepsilon_{2,6} \\ \varepsilon_{3,0} & \varepsilon_{3,1} & \varepsilon_{3,2} & \varepsilon_{3,3} & \varepsilon_{3,4} & \varepsilon_{3,5} & \varepsilon_{3,6} \\ \varepsilon_{4,0} & \varepsilon_{4,1} & \varepsilon_{4,2} & \varepsilon_{4,3} & \varepsilon_{4,4} & \varepsilon_{4,5} & \varepsilon_{4,6} \\ \varepsilon_{5,0} & \varepsilon_{5,1} & \varepsilon_{5,2} & \varepsilon_{5,3} & \varepsilon_{5,4} & \varepsilon_{5,5} & \varepsilon_{5,6} \\ \varepsilon_{6,0} & \varepsilon_{6,1} & \varepsilon_{6,2} & \varepsilon_{6,3} & \varepsilon_{6,4} & \varepsilon_{6,5} & \varepsilon_{6,6} \end{bmatrix} \tag{17a}$$

$$[\varepsilon_{xx}]_{\text{Img}(-1)} = \begin{bmatrix} 0 & \varepsilon_{0,-1} & \varepsilon_{0,-2} & \varepsilon_{0,-3} & \varepsilon_{0,-4} & \varepsilon_{0,-5} & \varepsilon_{0,-6} \\ 0 & \varepsilon_{1,-1} & \varepsilon_{1,-2} & \varepsilon_{1,-3} & \varepsilon_{1,-4} & \varepsilon_{1,-5} & \varepsilon_{1,-6} \\ 0 & \varepsilon_{2,-1} & \varepsilon_{2,-2} & \varepsilon_{2,-3} & \varepsilon_{2,-4} & \varepsilon_{2,-5} & \varepsilon_{2,-6} \\ 0 & \varepsilon_{3,-1} & \varepsilon_{3,-2} & \varepsilon_{3,-3} & \varepsilon_{3,-4} & \varepsilon_{3,-5} & \varepsilon_{3,-6} \\ 0 & \varepsilon_{4,-1} & \varepsilon_{4,-2} & \varepsilon_{4,-3} & \varepsilon_{4,-4} & \varepsilon_{4,-5} & 0 \\ 0 & \varepsilon_{5,-1} & \varepsilon_{5,-2} & \varepsilon_{5,-3} & \varepsilon_{5,-4} & 0 & 0 \\ 0 & \varepsilon_{6,-1} & \varepsilon_{6,-2} & \varepsilon_{6,-3} & 0 & 0 & 0 \end{bmatrix} \tag{17b}$$

$$[\varepsilon_{xx}]_{\text{Img}(+1)} = \begin{bmatrix} 0 & 0 & 0 & \varepsilon_{0,9} & \varepsilon_{0,8} & \varepsilon_{0,7} & 0 \\ 0 & 0 & \varepsilon_{1,10} & \varepsilon_{1,9} & \varepsilon_{1,8} & \varepsilon_{1,7} & 0 \\ 0 & \varepsilon_{2,11} & \varepsilon_{2,10} & \varepsilon_{2,9} & \varepsilon_{2,8} & \varepsilon_{2,7} & 0 \\ \varepsilon_{3,12} & \varepsilon_{3,11} & \varepsilon_{3,10} & \varepsilon_{3,9} & \varepsilon_{3,8} & \varepsilon_{3,7} & 0 \\ \varepsilon_{4,12} & \varepsilon_{4,11} & \varepsilon_{4,10} & \varepsilon_{4,9} & \varepsilon_{4,8} & \varepsilon_{4,7} & 0 \\ \varepsilon_{5,12} & \varepsilon_{5,11} & \varepsilon_{5,10} & \varepsilon_{5,9} & \varepsilon_{5,8} & \varepsilon_{5,7} & 0 \\ \varepsilon_{6,12} & \varepsilon_{6,11} & \varepsilon_{6,10} & \varepsilon_{6,9} & \varepsilon_{6,8} & \varepsilon_{6,7} & 0 \end{bmatrix} \tag{17c}$$

$$[\varepsilon_{xx}]_{\text{Img}(-2)} = \begin{bmatrix} 0 & 0 & 0 & \varepsilon_{0,-9} & \varepsilon_{0,-8} & \varepsilon_{0,-7} & 0 \\ 0 & 0 & 0 & 0 & \varepsilon_{1,-8} & \varepsilon_{1,-7} & 0 \\ 0 & 0 & 0 & 0 & 0 & \varepsilon_{2,-7} & 0 \\ 0 & 0 & 0 & 0 & 0 & 0 & 0 \\ 0 & 0 & 0 & 0 & 0 & 0 & 0 \\ 0 & 0 & 0 & 0 & 0 & 0 & 0 \\ 0 & 0 & 0 & 0 & 0 & 0 & 0 \end{bmatrix} \tag{17d}$$

$$[\varepsilon_x]_{\text{Img}(+2)} = \begin{bmatrix} 0 & 0 & 0 & 0 & 0 & 0 & 0 \\ 0 & 0 & 0 & 0 & 0 & 0 & 0 \\ 0 & 0 & 0 & 0 & 0 & 0 & 0 \\ 0 & 0 & 0 & 0 & 0 & 0 & 0 \\ 0 & \varepsilon_{4,13} & 0 & 0 & 0 & 0 & 0 \\ 0 & \varepsilon_{5,13} & \varepsilon_{5,14} & 0 & 0 & 0 & 0 \\ 0 & \varepsilon_{6,13} & \varepsilon_{6,14} & \varepsilon_{6,15} & 0 & 0 & 0 \end{bmatrix} \tag{17e}$$

where (17a) is associated with the original structure, while (17b)–(17e) are contributed by the image regions. As seen from the above equation, these latter contributions to the equivalent permittivity matrix decreases dramatically with the increase in the number of image regions (Img). Since the elements of the equivalent permittivity matrix only depend on the basis functions and the material properties of the structure, both the $[\hat{\varepsilon}_{xx}]$ and its inverse $[\hat{\varepsilon}_{xx}]^{-1}$ can be computed in advance and saved in the MRTD Maxwell solver for the update equations. Consequently, the E-field can be updated as follows:

$$\phi x E^n_{i+\frac{1}{2},j,k} = \frac{1}{\varepsilon_0} \sum_{j'=0}^{N_y} \left([\hat{\varepsilon}_{xx}]^{-1} \right)_{j,j'} \phi x D^n_{i+\frac{1}{2},j',k} \tag{18}$$

where, we apparently only need to compute the product of two small matrices, whose dimensions are typically six or less in this study, to update the E-fields at each time step.

C. MIT in Update Equations

Although, in principle, (6) and (7) can be employed to update the fields, they are numerically inefficient and somewhat impractical for coding and computation because the summations in these update expressions include both the original and image regions. In this section, we truncate the summations in these update equations by excluding some of the image field quantities. This is accomplished by carrying out the following two steps.

Step 1) Express all the field quantities in terms of those defined in the original structure by the MIT technique described in the previous section.

Step 2) Maintain the values and positions of the coefficients $a(\nu)$ unchanged for all of the terms, but express them only by using the grid indices inside the structure.

Following this procedure, we can rewrite the update equations for the x-components using the MIT in (19a) and (19b), shown at the bottom of the following page, where N_y and N_z are the numbers of cells along the y- and z-directions inside the structure, respectively, and the summation indexes [*odd* $(1, 3, \ldots)$ and *even* $(2, 4, \ldots)$] denote the contributions to the updated field quantities from the specified odd or even image regions, respectively.

Before concluding this section, it would be worthwhile to point out that although (19a) and (19b) are quite lengthy, they are actually quite efficient from the point-of-view of coding and computation. Since all of the field quantities usually have small dimensions, the coefficients $a(\nu)$ can be computed in advance and saved in the MRTD solver for later use.

$$
\begin{aligned}
{}_{\phi x}D^{n}_{i+\frac{1}{2},j,k} = {}_{\phi x}D^{n}_{i+\frac{1}{2},j,k} + \Bigg\{ & \sum_{\nu=0}^{N_y-1} a(\nu-j)\, {}_{\phi z}H^{n+\frac{1}{2}}_{i+\frac{1}{2},\nu+\frac{1}{2},k} + \Bigg[\sum_{\mathrm{Img}=\mathrm{even}} \Bigg(\sum_{\nu=0}^{N_y-1} a(-(\mathrm{Img}-2)\cdot N_y - \nu - j - 1) \\
& + \sum_{\nu=0}^{N_y-1} a(\mathrm{Img}\cdot N_y + \nu - j) \Bigg)\, {}_{\phi z}H^{n+\frac{1}{2}}_{i+\frac{1}{2},\nu+\frac{1}{2},k} \Bigg] \\
& + \Bigg[\sum_{\mathrm{Img}=\mathrm{odd}} \Bigg(\sum_{\nu=0}^{N_y-1} a(-\mathrm{Img}\cdot N_y - \nu - j - 1) + \sum_{m=0}^{N_y-1} a(\mathrm{Img}\cdot N_y + \nu - j) \Bigg) \\
& \times {}_{\phi z}H^{n+\frac{1}{2}}_{i+\frac{1}{2},N_y-\nu-1+\frac{1}{2},k} \Bigg] \Bigg\} \frac{\Delta t}{\Delta y} \\
& + \Bigg\{ \sum_{\nu=0}^{N_z-1} a(\nu-k)\, {}_{\phi y}H^{n+\frac{1}{2}}_{i+\frac{1}{2},j,\nu+\frac{1}{2}} + \Bigg[\sum_{\mathrm{Img}=\mathrm{even}} \Bigg(\sum_{\nu=0}^{N_z-1} a(-(\mathrm{Img}-2)\cdot N_z - \nu - k - 1) \\
& + \sum_{\nu=0}^{N_z-1} a(\mathrm{Img}\cdot N_z + \nu - k) \Bigg)\, {}_{\phi y}H^{n+\frac{1}{2}}_{i+\frac{1}{2},j,\nu+\frac{1}{2}} \Bigg] \\
& + \Bigg[\sum_{\mathrm{Img}=\mathrm{odd}} \Bigg(\sum_{\nu=0}^{N_z-1} a(-\mathrm{Img}\cdot N_z - \nu - k - 1) + \sum_{\nu=0}^{N_z-1} a(\mathrm{Img}\cdot N_z + \nu - k) \Bigg) \\
& \times {}_{\phi y}H^{n+\frac{1}{2}}_{i+\frac{1}{2},j,N_z-\nu-1+\frac{1}{2}} \Bigg] \Bigg\} \frac{\Delta t}{\Delta z}
\end{aligned}
\tag{19a}
$$

$$
\begin{aligned}
H^{n+\frac{1}{2}}_{i,j+\frac{1}{2},k+\frac{1}{2}} = {}_{\phi x}H^{n-\frac{1}{2}}_{i,j+\frac{1}{2},k+\frac{1}{2}} + \frac{1}{\mu_0} \Bigg\{ & \sum_{\nu=0}^{N_z} a(\nu-k-1)\, {}_{\phi y}E^{n}_{i,j+\frac{1}{2},\nu} + \Bigg[\sum_{\mathrm{Img}=\mathrm{even}} \Bigg(-\sum_{\nu=0}^{N_z-1} a(-(\mathrm{Img}-2)\ N_z - \nu - k - 2) \\
& + \sum_{m=0}^{N_z-1} a(\mathrm{Img}\cdot N_z + \nu - k) \Bigg)\, {}_{\phi y}E^{n}_{i,j+\frac{1}{2},\nu+1} \Bigg] \\
& + \Bigg[\sum_{\mathrm{Img}=\mathrm{odd}} \Bigg(\sum_{\nu=0}^{N_z-1} a(-\mathrm{Img}\cdot N_z - \nu - k - 2) - \sum_{\nu=0}^{N_z-1} a(\mathrm{Img}\cdot N_z + \nu - k) \Bigg) \\
& \times {}_{\phi z}E^{n+\frac{1}{2}}_{i,j+\frac{1}{2},N_z-\nu-1} \Bigg] \Bigg\} \frac{\Delta t}{\Delta z} \\
& - \frac{1}{\mu_0} \Bigg\{ \sum_{\nu=0}^{N_y} a(\nu-j-1)\, {}_{\phi z}E^{n}_{i,\nu,k+\frac{1}{2}} + \Bigg[\sum_{\mathrm{Img}=\mathrm{even}} \Bigg(-\sum_{\nu=0}^{N_y-1} a(-(\mathrm{Img}-2)\ N_y - \nu - j - 2) \\
& + \sum_{\nu=0}^{N_y-1} a(\mathrm{Img}\cdot N_y + \nu - j) \Bigg)\, {}_{\phi z}E^{n}_{i,\nu+1,k+\frac{1}{2}} \Bigg] \\
& + \Bigg[\sum_{\mathrm{Img}=\mathrm{odd}} \Bigg(\sum_{\nu=0}^{N_y-1} a(-\mathrm{Img}\cdot N_y - \nu - j - 2) - \sum_{\nu=0}^{N_y-1} a(\mathrm{Img}\cdot N_y + \nu - j) \Bigg) \\
& \times {}_{\phi z}E^{n}_{i,N_y-\nu-1,k+\frac{1}{2}} \Bigg] \Bigg\} \frac{\Delta t}{\Delta y}
\end{aligned}
\tag{19b}
$$

III. 2-D MRTD Analysis for Printed Transmission Lines

A. Field Construction

Following the procedure described in [10] and [11], we begin the 2-D MRTD analysis by deriving a set of governing equations for the problem at hand, i.e., the lossless guided-wave structure, shown in Fig. 3. We begin by expanding the field quantities as

$$\left\{ \begin{array}{l} E_x(x,y,z,t), E_y(x,y,z,t), E_z(x,y,z,t) \\ H_x(x,y,z,t), H_y(x,y,z,t), H_z(x,y,z,t) \end{array} \right\}^t = \left\{ \begin{array}{l} jE_x(x,y,t), jE_y(x,y,t), E_z(x,y,t) \\ H_x(x,y,t), H_y(x,y,t), jH_z(x,y,t) \end{array} \right\}^t e^{-j\beta z} \quad (20)$$

where β is the propagation constant for the structure. Next, we use GDMOs to obtain the following governing equations from the Maxwell's curl equations:

$$\begin{bmatrix} 0 & j\beta & \partial_y \\ -j\beta & 0 & -\partial_x \\ -\partial_y & \partial_x & 0 \end{bmatrix} \begin{bmatrix} H_x \\ H_y \\ 0 \end{bmatrix} = \left(\varepsilon_0 \frac{\partial}{\partial t} \begin{bmatrix} \varepsilon_{xx} & 0 & 0 \\ 0 & \varepsilon_{yy} & 0 \\ 0 & 0 & \varepsilon_{zz} \end{bmatrix} + \begin{bmatrix} \sigma_x^e & 0 & 0 \\ 0 & \sigma_y^e & 0 \\ 0 & 0 & \sigma_z^e \end{bmatrix} \right) \times \begin{bmatrix} jE_x \\ jE_y \\ E_z \end{bmatrix} \quad (21a)$$

$$\begin{bmatrix} 0 & j\beta & \partial_y \\ -j\beta & 0 & -\partial_x \\ -\partial_y & \partial_x & 0 \end{bmatrix} \begin{bmatrix} jE_x \\ jE_y \\ E_z \end{bmatrix} = \left(-\mu_0 \frac{\partial}{\partial t} \begin{bmatrix} \mu_{xx} & 0 & 0 \\ 0 & \mu_{yy} & 0 \\ 0 & 0 & \mu_{zz} \end{bmatrix} + \begin{bmatrix} \sigma_x^m & 0 & 0 \\ 0 & \sigma_y^m & 0 \\ 0 & 0 & \sigma_z^m \end{bmatrix} \right) \times \begin{bmatrix} H_x \\ H_y \\ jH_z \end{bmatrix}. \quad (21b)$$

In practice, we set $\sigma_\alpha^m = 0$. Note that a printed planar transmission line is usually inhomogeneous in the vertical direction, but homogenous in the horizontal direction, which leads to $\varepsilon_{\alpha\alpha} = \varepsilon_{\alpha\alpha}(y), (\alpha = x, y, z)$.

B. 2-D MRTD Algorithm

Next, we represent all the field quantities by using scaling functions in space and pulse functions in time. For instance, for the x-component of the fields, we write

$$E_x(x,y,t) = \sum_{n,i,j=-\infty}^{+\infty} \phi_x E_{i+\frac{1}{2},j}^n \phi_{i+\frac{1}{2}}(x) \phi_j(y) h_n(t) \quad (22)$$

$$H_x(x,y,t) = \sum_{n,i,j=-\infty}^{+\infty} \phi_x H_{i,j+\frac{1}{2}}^{n+\frac{1}{2}} \phi_i(x) \phi_{j+\frac{1}{2}}(y) h_{n+\frac{1}{2}}(t). \quad (23)$$

Substitution of the field expansions into Maxwell's equations, followed by the application of the Galerkin's method, leads us to obtain a set of field update equations. For instance, the x-components of the update equations are given by

$$\phi_x H_{i,j+\frac{1}{2}}^{n+\frac{1}{2}} = \phi_x H_{i,j+\frac{1}{2}}^{n-\frac{1}{2}} + \frac{\Delta t}{\mu_0 \mu_x} \left[\beta_{\phi y} E_{i,j+\frac{1}{2}}^n - \sum_\nu a(\nu) \phi_z E_{i,j+\nu+1}^n \frac{1}{\Delta y} \right] \quad (24)$$

$$\sum_{i',j'=-\infty}^{+\infty} (\sigma_x^e)_{ii',jj'} \frac{\Delta t}{2} \left(\phi_x E_{i'+\frac{1}{2},j'}^{n+1} + \phi_x E_{i'+\frac{1}{2},j'}^n \right) + \varepsilon_0 \sum_{j'=-\infty}^{+\infty} (\varepsilon_{xx})_{j,j'} \left(\phi_x E_{i+\frac{1}{2},j'}^{n+1} - \phi_x E_{i+\frac{1}{2},j'}^n \right) = \Delta t \left[\beta_{\phi y} H_{i+\frac{1}{2},j}^{n+\frac{1}{2}} + \sum_m a(m) \phi_z H_{i+\frac{1}{2},j+m+1}^{n+\frac{1}{2}} \frac{1}{\Delta y} \right] \quad (25)$$

where the coefficient $a(\nu)$ is given in [1]. Assuming the conducting strip is infinitely thin, we can express its conductivity

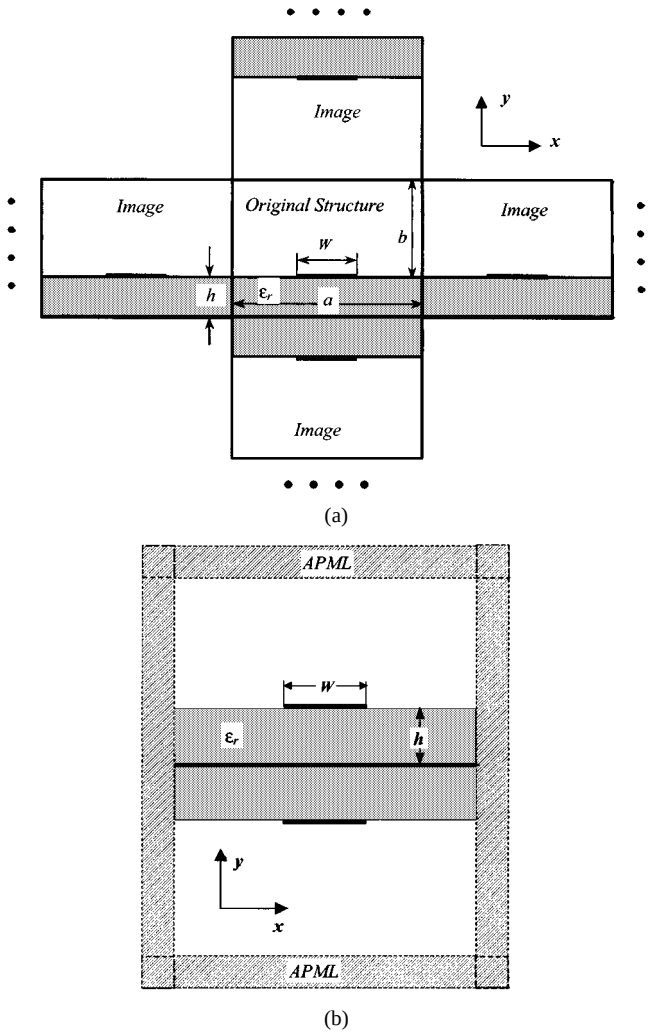

Fig. 3. Cross section of the printed transmission lines and their images. (a) Shielded microstrip line. (b) Open microstrip line.

in (26), shown at the bottom of this page. Thus, we can express $(\varepsilon_{xx})_{j,j'}$ and $(\sigma_x^e)_{ii',jj'}$ as

$$(\varepsilon_{xx})_{j,j'} = \int_{-\infty}^{+\infty} \phi_j(y)\varepsilon_{xx}(y)\phi_{j'}(y)\,\frac{dy}{\Delta y} \tag{27a}$$

$$(\sigma_x^e)_{ii',jj'} = \int_{-\infty}^{+\infty}\int_{-\infty}^{+\infty} \phi_{i+\frac{1}{2}}(x)\phi_j(y)\sigma\phi_{i'+\frac{1}{2}}(x) \times \phi_{j'}(y)\,\frac{dx\,dy}{\Delta x\Delta y}. \tag{27b}$$

By considering image contributions and using the first-order approximation, we can derive

$$(\sigma_x^e)_{ii',jj'} = \sigma_{i,i'}\delta_{i,i'}\varsigma_{j,j'}\delta_{j,j'}\left(\delta_{j,j_0} + \delta_{j,-j_0} + \delta_{j,2j_0} + \cdots\right) \tag{28}$$

where $\delta_{ii'}$ is the Kronecker symbol, which is one for $i = i'$, otherwise 0. Then, we further rewrite the discretized time-domain equation as

$$\begin{aligned}&\left(\phi x E_{i+\frac{1}{2},j}^{n+1} + \phi x E_{i+\frac{1}{2},j}^{n}\right) \times \frac{\sigma^e\left(\delta_{j,j_0} + \delta_{j,-j_0} + \delta_{j,2j_0} + \cdots\right)\Delta t}{2} \\ &\quad + \varepsilon_0 \sum_{j'=-\infty}^{+\infty} (\varepsilon_{xx})_{j,j'}\left(\phi x E_{i+\frac{1}{2},j'}^{n+1} - \phi x E_{i+\frac{1}{2},j'}^{n}\right) \\ &\quad = \Delta t\left[\beta_{\phi y} H_{i+\frac{1}{2},j}^{n+\frac{1}{2}} + \sum_{\nu} a(\nu)_{\phi z} H_{i+\frac{1}{2},j+\nu+1}^{n+\frac{1}{2}}\frac{1}{\Delta y}\right].\end{aligned} \tag{29}$$

The summation index ν in (29) not only includes the regions in the interior of the original structure, but also the image regions. Two types of boundaries are frequently used for truncating the grids, i.e., the absorbing boundary condition for open structures and the PEC for shielded ones. The PEC boundary is usually handled by using the MIT described earlier. Fig. 3 shows the original structures, i.e., shielded and open microstrip lines, as well as their images. By taking an inverse of the following:

$$\begin{aligned}&\left(\phi x E_{i+\frac{1}{2},j}^{n+1} + \phi x E_{i+\frac{1}{2},j}^{n}\right)\frac{\sigma^e\delta_{j,j_0}\Delta t}{2} \\ &\quad + \varepsilon_0 \sum_{j'=0}^{N_y} (\hat{\varepsilon}_{xx})_{j,j'}\left(\phi x E_{i+\frac{1}{2},j'}^{n+1} - \phi x E_{i+\frac{1}{2},j'}^{n}\right) \\ &\quad = \Delta t\left[\beta_{\phi y} H_{i+\frac{1}{2},j}^{n+\frac{1}{2}} + \sum_{\nu} a(\nu)_{\phi z} H_{i+\frac{1}{2},j+\nu+1}^{n+\frac{1}{2}}\frac{1}{\Delta y}\right]\end{aligned} \tag{30}$$

we can obtain the update equation for the x-component of the E-field as follows:

$$\begin{aligned}&\phi x E_{i+\frac{1}{2},j}^{n+1} \\ &\quad = \sum_{j'=0}^{N_y} \left([A]\right)_{j,j'} \phi x E_{i+\frac{1}{2},j'}^{n} \\ &\qquad + \frac{1}{\varepsilon_0}\sum_{j'=0}^{N_y}\left([B]\right)_{j,j'}\left[\beta_{\phi y} H_{i+\frac{1}{2},j'}^{n+\frac{1}{2}}\Delta t + \sum_{m} a(m)_{\phi z} H_{i+\frac{1}{2},j'+m+1}^{n+\frac{1}{2}}\frac{\Delta t}{\Delta y}\right]\end{aligned} \tag{31}$$

with

$$[A] = \left[[\hat{\varepsilon}_{xx}]_{j,j'} + [I]\frac{\sigma^e\delta_{j,j_0}\Delta t}{2\varepsilon_0}\right]^{-1} \cdot \left[[\hat{\varepsilon}_{xx}]_{j,j'} - [I]\frac{\sigma^e\delta_{j,j_0}\Delta t}{2\varepsilon_0}\right] \tag{32a}$$

$$[B] = \left[[\hat{\varepsilon}_{xx}]_{j,j'} + [I]\frac{\sigma^e\delta_{j,j_0}\Delta t}{2\varepsilon_0}\right]^{-1}. \tag{32b}$$

For a shielded structure, we need to employ the MIT for constructing the $[\hat{\varepsilon}_{xx}]$ matrix. Since the matrix $[A]$ and $[B]$ only depend on the basis functions and the material properties of the structure, they can be computed in advance and saved in the MRTD Maxwell solver for the update equations.

C. Application of APML

Here, we address the problem of mesh truncation for open structures. We find that the 2-D version of the lossy uniaxial APML [12] medium is well suited for this purpose. Since the APML is applied only in the x- and y-directions, the frequency-domain Maxwell's curl equation in the APML medium can be written as

$$\begin{aligned}&\begin{bmatrix} j\dfrac{\partial H_z}{\partial y} + j\beta H_y \\ -j\beta H_x - j\dfrac{\partial H_z}{\partial x} \\ \dfrac{\partial H_y}{\partial x} - \dfrac{\partial H_x}{\partial y}\end{bmatrix} \\ &\quad = j\omega\varepsilon_0\begin{bmatrix}\dfrac{\varepsilon_{xx}s_y}{s_x} & 0 & 0 \\ 0 & \dfrac{\varepsilon_{yy}s_x}{s_y} & 0 \\ 0 & 0 & \varepsilon_{zz}s_xs_y\end{bmatrix}\begin{bmatrix}jE_x \\ jE_y \\ E_z\end{bmatrix}\end{aligned} \tag{33a}$$

$$\sigma_\alpha^e = \begin{cases}\sigma, & i_1\Delta x \le x \le i_2\Delta x,\ \left(j_0\Delta y - \dfrac{\tau}{2}\right) < y < \left(j_0\Delta y + \dfrac{\tau}{2}\right) \quad (\Delta = x, y) \\ 0, & \text{otherwise}\end{cases} \tag{26}$$

$$\begin{bmatrix} \dfrac{\partial E_z}{\partial y}+\beta E_y \\ \beta E_x-\dfrac{\partial E_z}{\partial x} \\ j\dfrac{\partial E_y}{\partial x}-j\dfrac{\partial E_x}{\partial y} \end{bmatrix} = -j\omega\mu_0 \begin{bmatrix} \dfrac{\mu_{xx}s_y}{s_x} & 0 & 0 \\ 0 & \dfrac{\mu_{yy}s_x}{s_y} & 0 \\ 0 & 0 & \mu_{zz}s_xs_y \end{bmatrix} \begin{bmatrix} H_x \\ H_y \\ jH_z \end{bmatrix} \quad (33b)$$

with

$$s_\alpha = \begin{cases} 1+\dfrac{\sigma_\alpha}{j\omega\varepsilon_0}, & \text{for absorption in } \alpha \text{ direction} \\ 1, & \text{elsewhere} \end{cases} \qquad (\alpha = x, y). \quad (34)$$

Depending on combination of the values of s_x and s_y, the above Maxwell's equations are applicable to all of the APML regions, which include two side edges, the top wall, as well as the two corners. By expanding the above equations for the case of the corners, we immediately obtain the x-components of the following governing equations:

$$\frac{\partial H_z}{\partial y}-\frac{\partial H_y}{\partial z}=j\omega D_x+\frac{\sigma_y}{\varepsilon_0}D_x \quad (35)$$

$$\frac{\partial E_z}{\partial y}-\frac{\partial E_y}{\partial z}=-j\omega B_x-\frac{\sigma_y}{\varepsilon_0}B_x. \quad (36)$$

Here, we use a two-step update approach to time-stepping fields inside APML regions. Following the MRTD discretization procedure described previously, we obtain the desired E-field update equations

$$\begin{aligned} {}_{\phi x}D^{n+1}_{i+\frac{1}{2},j} &= \frac{1-\dfrac{\sigma_y\Delta t}{2\varepsilon_0}}{1+\dfrac{\sigma_y\Delta t}{2\varepsilon_0}}\,{}_{\phi x}D^{n}_{i+\frac{1}{2},j} \\ &\quad+\frac{1}{1+\dfrac{\sigma_y\Delta t}{2\varepsilon_0}}\left(\beta_{\phi y}H^{n+\frac{1}{2}}_{i+\frac{1}{2},j}\Delta t \right. \\ &\quad\left. +\sum_m a(m)_{\phi z}H^{n+\frac{1}{2}}_{i+\frac{1}{2},j+m+1}\frac{\Delta t}{\Delta y}\right) \end{aligned} \quad (37)$$

$$\begin{aligned} {}_{\phi x}E^{n+1}_{i+\frac{1}{2},j} &= {}_{\phi x}E^{n}_{i+\frac{1}{2},j}+\frac{1}{\varepsilon_0}\sum_{j'}\left([\varepsilon_x]^{-1}\right)_{j,j'} \\ &\quad\times\left[\left(1+\frac{\sigma_x\Delta t}{2\varepsilon_0}\right){}_{\phi x}D^{n+1}_{i+\frac{1}{2},j'} \right. \\ &\quad\left. -\left(1-\frac{\sigma_x\Delta t}{2\varepsilon_0}\right){}_{\phi x}D^{n}_{i+\frac{1}{2},j'}\right]. \end{aligned} \quad (38)$$

We can employ the same procedure to obtain the remaining E- and H-field update equations.

In applications of the MRTD method, we chose the time step Δt to satisfy the stability and limit condition [1] in all simulations. Starting from the convergence condition of the above update equations of the D-fields, we have empirically proven that, to obtain good absorption, the APML parameters may be chosen as follows:

$$\sigma_\alpha=\sigma_{\max}\left|\frac{\alpha-\alpha_0}{N_p\Delta\alpha}\right|^p=\gamma\frac{\varepsilon_0}{\Delta t}\left|\frac{i-i_0}{N_p}\right|^p, \qquad (\alpha=x,y) \quad (39)$$

where α_0 is the starting position in the α direction, d is the thickness of the APML, and N_p is the number of cells within the APML region. In principle, it can be shown that this relationship is consistent with the standard form, which can be derived from a plane wave, normally incidence on a PML region. We found that we can minimize the reflection error, and have good absorption, if we choose $p=2$ and $\gamma=0.8$–1.6.

D. Computation of the Propagation Characteristic

Typically, for the printed transmission lines, the two parameters of interest are the effective dielectric constant ε_{eff} and the characteristic impedance Z_0, which can, in general, be derived from the MRTD calculated field quantities. For example, the time-domain voltage V defined as an integral from the PEC ground to the strip line can be calculated as follows:

$$\begin{aligned} V &= -\int_0^h E_y(x_0,y,t_0)\,dy \\ &= -\sum_{l=0}^{N_s}\int_{l\Delta y}^{(l+1)\Delta y} E_y(x_0,y,t_0)\,dy \\ &= -\sum_{l=0}^{N_s}\int_{l\Delta y}^{(l+1)\Delta y}\left[\int\int E_y(x,y,t)\delta(x-x_0)\right. \\ &\qquad\left.\times\,\delta(t-t_0)\,dx\,dt\right]dy \\ &= -\sum_{l=0}^{N_s}\left[\sum_{i,j-l=-\infty}^{\infty}{}_{\phi y}E^n_{i,j-l+\frac{1}{2}}\phi_i(x_0)b(j)\Delta y\right] \end{aligned} \quad (40)$$

where N_s is the number of the cells from the bottom ground to the PEC strip, and the indexes i and j of the summation span the original microstrip line and its image regions. The integral coefficient $b(j)$ forms a localized distribution with the even symmetric $b(j)=b(-j)$ listed in Table I. We can apply a similar procedure to solve for all required field quantities.

E. BHW Function Truncation and Modulation

To eliminate the Gibb's phenomenon that results from an abrupt truncation of the time-domain response, Blackman–Harris (BH) window function is used to truncate and modulate the time domain [11]. We write

$$\left[E^W_\kappa(t_n),H^W_\kappa(t_n)\right]=\left[E_\kappa(t_n),H_\kappa(t_n)\right]W_{\text{BH}}(t_n), \qquad (\kappa=x,y,z) \quad (41)$$

where $[E_\kappa(t_n),H_\kappa(t_n)]$ represents the original time-domain electromagnetic fields defined in the MRTD algorithm, and $[E^W_\kappa(t_n),H^W_\kappa(t_n)]$ are the windowed versions. Since the frequency-domain response is the convolution of the frequency-domain signature and its window function, the choice of the window function can significantly affect the accuracy of the propagation characteristics. Extremely low sidelobe

TABLE I
INTEGRAL COEFFICIENT $b(j)$

j	$b(j)$
0	0.9143952
1	0.0385998
2	0.0095740
3	-0.0086579
4	0.0050629
5	-0.0027034
6	0.0014053
7	-0.0007203
8	0.0000695

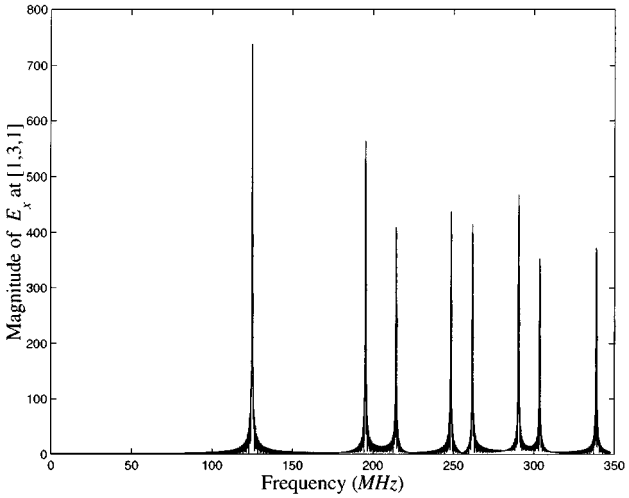

Fig. 4. Frequency spectrum of E_x at the location $[1, 3, 1]$ for an empty cavity.

levels (-92 dB) of the BH window ensures the accuracy of the extracted frequency-domain signals, while the use of the conventional rectangular window function, which has a much higher sidelobe level (-13 dB), can seriously corrupt the frequency signatures, especially for a resonant structure.

IV. NUMERICAL RESULTS

A. MIT–MRTD Application

We have applied the MRTD scheme in conjunction with the MIT to analyze a number of dielectric-loaded cavities, i.e., an empty cavity, two partially filled (25% and 50%) cavities containing a single dielectric medium, and two different two-layer dielectric-filled cavities. The dimensions of the cavity were set to be $1 \times 2 \times 1.5$ m^3 in the x-, y-, and z-directions, respectively, in all of these cases.

We begin with an empty cavity that is discretized with $2 \times 4 \times 3$ cells. The frequency spectrum of E_x sampled at the grid point $[1, 3, 1]$ is displayed in Fig. 4, and the extracted resonant frequencies for the dominant and higher order modes are summarized in Table II along with the discretization parameters. It is evident that the results obtained with the MRTD scheme show good agreement with both the analytical results and with those derived by using the FDTD. However, the MRTD scheme demands only 0.8% of the computational resources needed in the conventional FDTD technique. In addition, we have investigated the required CPU time for conventional MRTD and the

TABLE II
RESONANT FREQUENCIES IN MEGAHERTZ FOR AN EMPTY CAVITY
($V = 1 \times 2 \times 1.5$ m^3; $\Delta x = \Delta y = \Delta z = 1/2$ m)

Analytic	FDTD [1] ($10\times20\times15$)	S-MRTD [1] ($2\times4\times3$)	This Method ($2\times4\times3$)	Percentage Difference
125.00	124.85	125.10	124.95	-0.040%
180.27	179.75	180.50	180.39	0.067%
213.60	212.40	214.60	214.30	0.328%
246.22	244.50	248.70	248.55	0.946%
250.00	248.70	251.00	250.75	0.300%
301.04	298.95	303.90	303.65	0.580%
336.34	334.35	339.20	338.91	0.764%

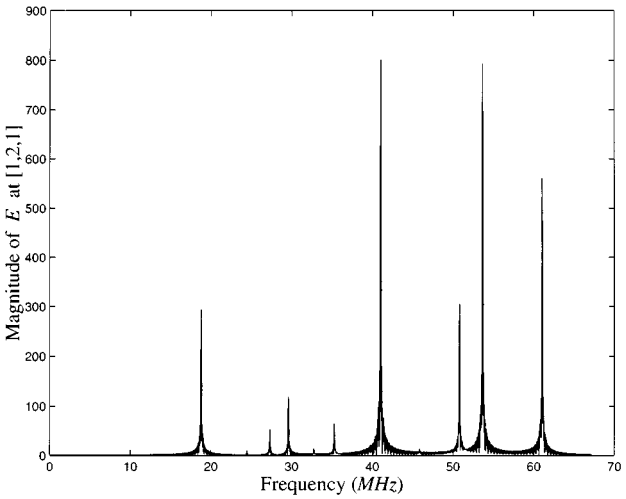

Fig. 5. Frequency spectrum of E_x at the location $[1, 2, 1]$ for a dielectric cavity with 50% filling.

MIT–MRTD schemes. For a total time step of $N_t = 10^4$, it is found that the CPU time for the conventional MRTD is about 19.27 s, while that of the MIT–MRTD requires about 27.08 s by using a 500-MHz Alpha digital workstation. Obviously, this increment of the CPU time is due to the use of additional images in the process of implementing the MIT–MRTD technique. Specially, we use five images along the positive and negative x-directions, and three in the remaining directions. By comparison, the conventional MRTD uses only a single image irrespective of the direction. We also note that the introduction of the MIT in the MRTD scheme enhances the accuracy of the results.

The MRTD analysis of the half- and quarter-filled dielectric cavities, with $\varepsilon_{r1} = \varepsilon_{r2} = 64$ and $\varepsilon_{r1} = 64, \varepsilon_{r2} = 1$, respectively, also yields excellent results, as is evident from Figs. 5 and 6 and Tables III and IV. Once again, the MRTD scheme is found to be highly efficient, when compared to the conventional FDTD method, since it requires only 0.8% and 1.2% of the CPU memory for the above two cases. The accuracy of the MRTD technique is again improved (except one frequency point) when it is combined with the MIT.

Next, we consider a two-layer dielectric-filled cavity using only $2 \times 6 \times 3$ cells to discretize the computational domain. We investigate the following two cases: $\varepsilon_{r1} = 64, \varepsilon_{r2} = 8$ and $\varepsilon_{r1} = 8, \varepsilon_{r2} = 64$ with $N_{y1} = N_{y2} = 1.5$ cells. The structure dimensions still remain $V = 1 \times 2 \times 1.5$ m^3. We also analyze the same problem using the traditional FDTD mesh with a discretization of $\Delta x = \Delta y = 2.5$ cm and $\Delta z = 3$ cm, i.e., $40 \times 40 \times 50$ cells. As seen from Figs. 7 and 8 and from Table V,

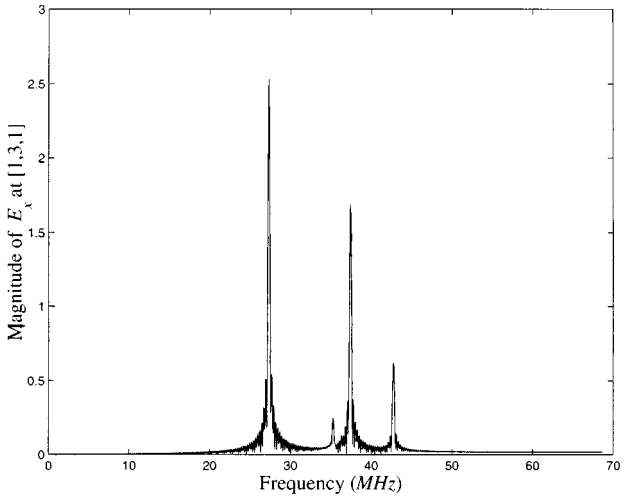

Fig. 6. Frequency spectrum of E_x at $[1, 3, 1]$ for a dielectric cavity with 25% filling.

TABLE III
RESONANT FREQUENCIES IN MEGAHERTZ FOR A PARTIALLY FILLED DIELECTRIC CAVITY WITH 50% FILLING ($\varepsilon_{r1} = \varepsilon_{r2} = 64; N_{y1} = N_{y2} = 1.5; V = 1 \times 2 \times 1.5$ m^3; $\Delta x = \Delta y = \Delta z = 1/2$ m)

Analytic	FDTD [1] (10×20×15)	S-MRTD [1] (2×4×3)	This Method (2×4×3)	Percentage Difference
18.627	18.615	18.715	18.692	0.349%
27.172	27.140	27.350	27.313	0.519%
29.375	29.215	29.580	29.526	0.514%
35.069	34.970	35.280	35.247	0.507%

TABLE IV
RESONANT FREQUENCIES IN MEGAHERTZ FOR A PARTIALLY FILLED DIELECTRIC CAVITY WITH 25% FILLING ($\varepsilon_{r1} = 64, \varepsilon_{r2} = 1; N_{y1} = N_{y2} = 1.5; V = 1 \times 2 \times 1.5$ m^3; $\Delta x = \Delta z = 1/2, \Delta y = 1/3$ m)

Analytic	FDTD [2] (10×20×15)	S-MRTD [2] (2×6×3)	This Method (2×6×3)	Percentage Difference
27.290	27.250	27.370	27.313	0.084%
37.136	37.000	37.370	37.323	0.503%
42.343	42.200	42.420	42.602	0.611%

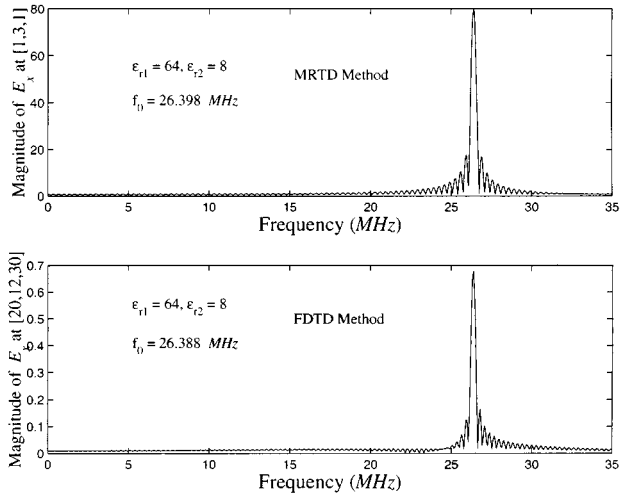

Fig. 7. Frequency spectrum of E_x of a two-layer dielectric-loaded cavity.

the two sets of computed results agree very well with each other and the percentage differences are 0.038% and 0.343%, for both

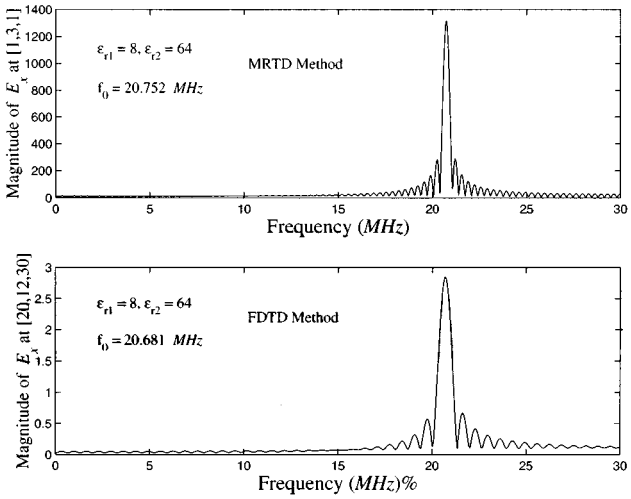

Fig. 8. Frequency spectrum of E_x for a two-layer dielectric-loaded cavity.

TABLE V
RESONANT FREQUENCIES IN MEGAHERTZ FOR A TWO-LAYER DIELECTRIC-FILLED CAVITY ($N_{y1} = N_{y2} = 1.5; V = 1 \times 2 \times 1.5$ m^3; $\Delta x = \Delta z = 1/2, \Delta y = 1/3$ m)

Case	FDTD (40×40×50)	This Method (2×6×3)	Percentage Difference
(*i*)	26.388	26.398	0.038%
(*ii*)	20.681	20.752	0.343%

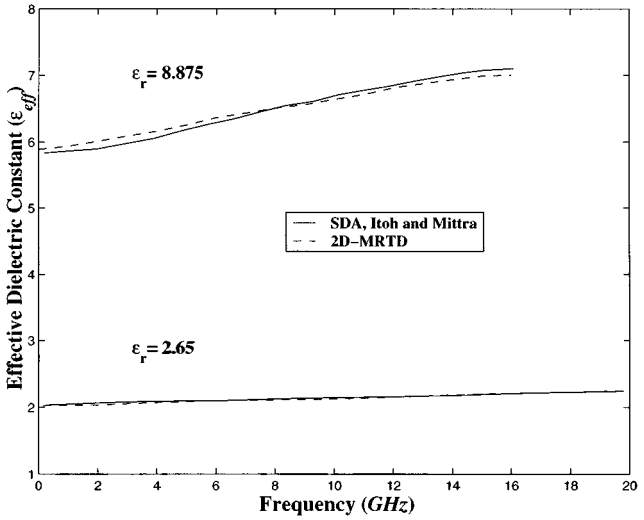

Fig. 9. Effective dielectric constant ε_{eff} versus frequency of a shielded microstrip line with $w = h = 1.27$, $a = b = 12.7$ mm.

cases, respectively. However, the MIT-MRTD scheme only uses 0.045% of the computational resources relative to the conventional FDTD algorithm.

B. 2-D MRTD Application

We consider a shielded microstrip line shown in Fig. 3(a), whose trace is assumed very thin and perfectly conducting. Fig. 9 shows that the propagation characteristics derived from an application of the present 2-D MRTD scheme agree quite well with those derived from the spectral-domain approach (SDA) [13].

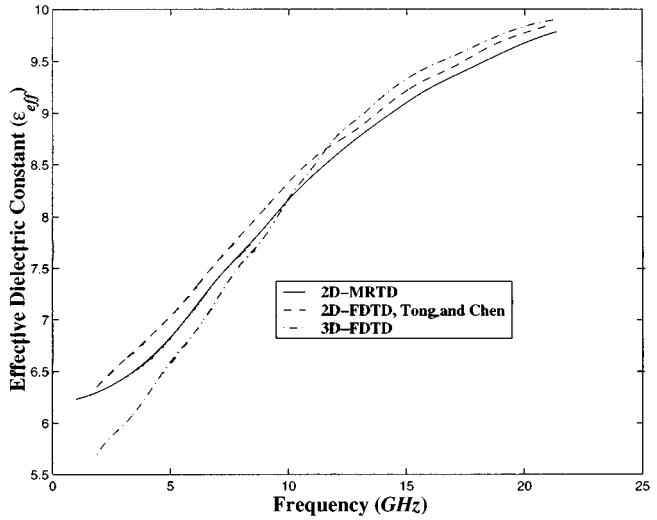

(a)

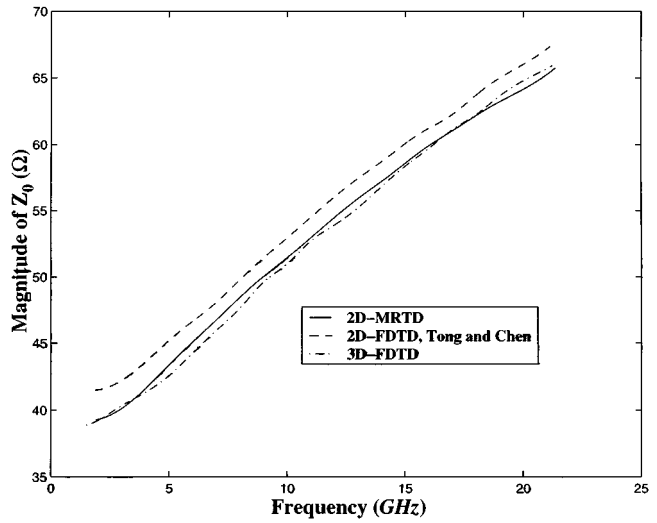

(b)

Fig. 10. Frequency dependence of propagation characteristics of a shielded microstrip line with $w = h = 1.5$, $a = 6.5$, $b = 3.5$ mm, $\varepsilon_{xx} = \varepsilon_{zz} = 9.4$, $\varepsilon_{yy} = 11.6$. (a) $\varepsilon_{\rm eff}$. (b) Magnitude of Z_0 in Ω.

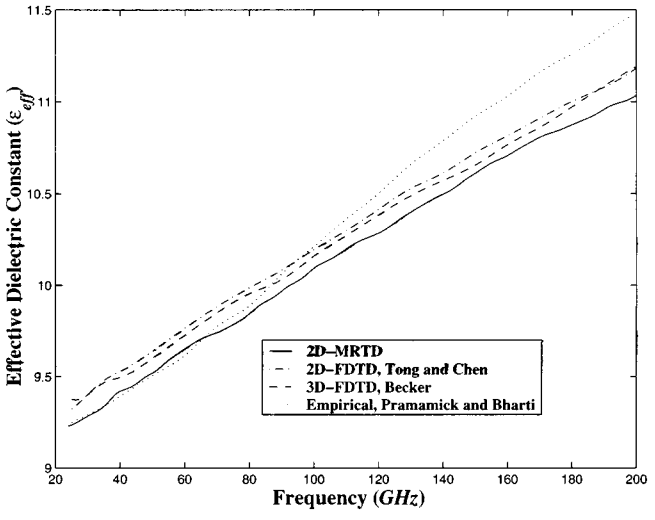

(a)

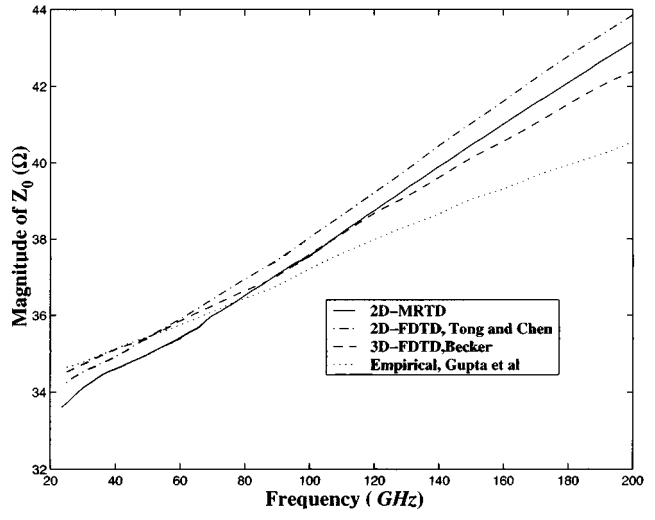

(b)

Fig. 11. Frequency dependence of propagation characteristics of an open microstrip line with $w/h = 1.5$, $h = 0.10$ mm, $\varepsilon_r = 13.3$. (a) $\varepsilon_{\rm eff}$. (b) Magnitude of Z_0 in Ω.

TABLE VI
DISCRETIZATION DIMENSIONS OF A SHIELDED MICROSTRIP LINE
($\varepsilon_{xx} = \varepsilon_{zz} = 9.4, \varepsilon_{yy} = 11.6$)

Method	Δx (*mm*)	Δy (*mm*)	N_x	N_y
2D-MRTD	0.5	0.5	13	7
2D-FDTD	0.125	0.125	52	28
3D-FDTD	0.125	0.125	52	28

TABLE VII
DISCRETIZATION DIMENSIONS OF AN OPEN MICROSTRIP LINE ($\varepsilon_r = 13.0$)

Method	Δx (*mm*)	Δy (*mm*)	N_x	N_y
2D-MRTD	0.05	0.0333	21	12
2D-FDTD	0.0125	0.0125	110	30
3D-FDTD	0.0125	0.0125	55	30

Next, we study the propagation characteristics of a shielded microstrip line, shown in Fig. 3(a), whose dimensions and substrate material are given in the caption of Fig. 10. We observe, from Fig. 10, that the MRTD-computed results are in good agreement with those published in the literature, derived by using the FDTD [11]. For this case, the distance from the air–dielectric interface of the structure to the inner surface of the APML is seven cells. The corresponding discretization parameters employed in the FDTD and MRTD methods are summarized in Table VI, and a comparison of the total number of cells needed in the MRTD and FDTD technique is presented in Table VI, and the relative advantage of the former is evident from the table.

Finally, we investigate an open microstrip line, whose geometry is specified in Fig. 3(b). Once again, from Fig. 11, we observe good agreement between the computed results and those derived by using the FDTD method [11], [14], as well as the empirical approach [15], [16]. The corresponding discretization parameters employed in the FDTD and MRTD methods are summarized Table VII. We note that the memory required in the 2-D MRTD method is only about 6.25% or 7.64% of the 2-D-FDTD

scheme for the same shielded and open microstrip lines, respectively. We further notice that, to ensure computational accuracy, we must employ at least two cells along the width of the narrow PEC strip.

V. Conclusion

In this paper we have presented an adjustable MIT, which can be incorporated in the MRTD scheme for the boundary truncation of PEC-shielded structures. We have also developed a 2-D version of the MRTD and have applied it in conjunction with an APML mesh truncation technique for the analysis of both shielded and open microstrip lines. We have developed a systematic technique for constructing the multiple images, extracting the constitutive relations, deriving the update equations, and determining the number of images in the transform domain of the MRTD. The propagation characteristics computed via the MRTD have been shown to be in good agreement with those obtained by using other numerical techniques. The computational resources needed in the MRTD scheme are only a small fraction of those of the FDTD algorithm, albeit the computational complexity is higher in the MRTD.

References

[1] M. Krumpholz and L. P. B. Katehi, "MRTD: New time domain schemes based on multiresolution analysis," *IEEE Trans. Microwave Theory Tech.*, vol. 44, pp. 555–571, Apr. 1996.

[2] R. Robertson, E. Tentzeris, M. Krumpholz, and L. P. B. Katehi, "MRTD analysis of dielectric cavity structures," in *IEEE MTT-S Int. Microwave Symp. Dig.*, 1996, pp. 1861–1864.

[3] E. Tentzeris, M. Krumpholz, and L. P. B. Katehi, "Application of MRTD to printed transmission lines," in *IEEE MTT-S Int. Microwave Symp. Dig.*, 1996, pp. 573–576.

[4] Q. Cao and Y. Chen, "MRTD analysis of a transient electromagnetic pulse propagating through a dielectric layer," *Int. J. Electron.*, vol. 86, pp. 459–474, Apr. 1999.

[5] R. L. Roberson, E. M. Tentzeris, M. Krumpholz, and L. P. B. Katehi, "Modeling of dielectric cavity structures using multiresolution time domain analysis," *Int. J. Numer. Modeling*, vol. 11, pp. 55–68, Apr. 1998.

[6] Y. Chen, K. Sun, B. Berker, and R. Mittra, "Unified matrix presentation of Maxwell's and wave equations using generalized different differential matrix operators," *IEEE Trans. Educ.*, vol. 41, pp. 61–69, Feb. 1998.

[7] G. Battle, "A block spin construction of ondelettes," *Commun. Math. Phys.*, vol. 67, pp. 601–615, 1987.

[8] P. G. Lemarie, "Ondelettes a localization exponentielle," *J. Math. Pures Applicat.*, vol. 67, pp. 277–236, 1988.

[9] R. F. Harrington, *Field Computation by Moment Methods*. Melbourne, FL: Krieger, 1982.

[10] S. Xiao and R. Vahldieck, "An efficient 2-D FDTD algorithm using real variables," *IEEE Microwave Guided Wave Lett.*, vol. 3, pp. 127–129, May 1993.

[11] M. Tong and Y. Chen, "Analysis of propagation characteristics and field images for printed transmission lines printed on anisotropic substrates using a 2D-FDTD method," *IEEE Trans. Microwave Theory Tech.*, vol. 46, pp. 1507–1510, Oct. 1998.

[12] S. D. Gedney, "An anisotropic perfectly matched layered-absorbing medium for the truncation of FDTD lattices," *IEEE Trans. Antennas Propagat.*, vol. 44, pp. 1630–1939, Dec. 1996.

[13] T. Itoh and R. Mittra, "A technique for computing dispersion characteristics of shielded microstrip line," *IEEE Trans. Microwave Theory Tech.*, vol. MTT-22, pp. 896–898, Oct. 1974.

[14] W. D. Becker, "The application of time-domain electromagnetic field solvers to computer package analysis and design," Ph.D. dissertation, Dept. Elect. Comput. Eng., Univ. Illinois at Urbana-Champaign, Urbana, IL, 1993.

[15] P. Pramanick and P. Bharti, "An accurate description of dispersion in microstrip," *Microwave J.*, pp. 89–96, Dec. 1981.

[16] K. C. Gupta, R. Grag, and R. Chadha, *Computer-Aided Design of Microwave Circuits*. Norwood, MA: Artech House, 1981.

Qunsheng Cao was born in Hefei, China, in 1959. He received the B.S. degree in physics from the University of Huainan Mining, Huainan, China, in 1982, and is currently working toward the Ph.D. degree in electronics and information engineering from the Hong Kong Polytechnic University, Hong Kong.

From 1989 to 1991, he was a Visiting Scholar with the Department of Physics, Wuhan University of Science and Technology, Wuhan, China. In 1994, he became an Associate Professor with the Wuhan University of Science and Technology. From 1996 to 1998, he was a Research Assistant with the Department of Electronic and Information Engineering (EIE), Hong Kong Polytechnic University. His current research interests include electromagnetic theories and applications, computational electromagnetic techniques, and, in particular, the MRTD scheme.

Yinchao Chen (M'94) received the Ph.D. degree in electrical engineering from the University of South Carolina, Columbia, in 1992.

During his earlier career in China, he was a Microwave and Antenna Engineer with the Nanjing Research Institute of Electronic Technology. From 1989 to 1995, he was a Teaching and Research Assistant, Post-Doctoral Fellow, Adjunct Assistant Professor, and Visiting Scholar Fellow with the University of South Carolina, South Carolina State University, and the University of Illinois at Urbana-Champaign, respectively. From October 1995 to June 2000, he was an Assistant Professor with the Department of Electronic and Information Engineering, Hong Kong Polytechnic University, Hong Kong. Since July 2000, he has been an Associate Professor with the Department of Electrical Engineering, University of South Carolina. His current research interests include computational electromagnetics with applications of millimeter-wave integrated circuits, wireless communication applications, electronic packaging modeling for VLSI devices, and microwave antenna applications. He has authored or co–authored 100 international publications in refereed journals and conference symposia and has contributed three book chapters.

Raj Mittra (S'54–M'57–SM'69–F'71–LF'96), photograph and biography not available at time of publication.